

Comparison of the signal-to-noise characteristics of quantum versus thermal ghost imaging

Malcolm N. O'Sullivan, Kam Wai Clifford Chan,* and Robert W. Boyd

Institute of Optics, University of Rochester, Rochester, New York 14627, USA

(Received 3 April 2010; published 4 November 2010)

We present a theoretical comparison of the signal-to-noise characteristics of quantum versus thermal ghost imaging. We first calculate the signal-to-noise ratio of each process in terms of its controllable experimental conditions. We show that a key distinction is that a thermal ghost image always resides on top of a large background; the fluctuations in this background constitutes an intrinsic noise source for thermal ghost imaging. In contrast, there is a negligible intrinsic background to a quantum ghost image. However, for practical reasons involving achievable illumination levels, acquisition times for thermal ghost images are often much shorter than those for quantum ghost images. We provide quantitative predictions for the conditions under which each process provides superior performance. Our conclusion is that each process can provide useful functionality, although under complementary conditions.

DOI: [10.1103/PhysRevA.82.053803](https://doi.org/10.1103/PhysRevA.82.053803)

PACS number(s): 42.50.Ar, 42.30.Va

I. INTRODUCTION

Ghost imaging is a procedure for forming the image of an object indirectly, by means of correlation measurements. It is called ghost imaging because the photons that provide the spatial information regarding the object have never directly interacted with the object to be imaged. Ghost imaging thus provides capabilities for image formation under unusual conditions, such as those that might apply for covert surveillance.

Two primary methods have emerged for forming ghost images. One is to make use of the correlations between photons produced by parametric down-conversion [1,2]. In this paper, we will refer to this method as quantum ghost imaging. The other method is to make use of the spatial correlations between two copies (usually formed by a beam splitter) of a speckle pattern or of a thermal light source [3,4]. In this paper we will refer to this method as thermal ghost imaging.

Both of these methods have proven useful in laboratory demonstrations of ghost imaging [1,4–12]. However, it is somewhat uncertain exactly what the trade-offs are between the two methods, and especially which one is expected to perform better under specified circumstances. In this paper, we perform calculations aimed at quantifying the performance of each of these methods. We note that related calculations have been presented by others [13–20].

Before we develop our detailed theoretical treatment of ghost imaging, we present here a qualitative comparison between these two methods.

Quantum ghost imaging makes use of the entangled photon pairs produced by spontaneous parametric down-conversion. As down-conversion tends to be an inefficient process, it produces a rather weak light source. In fact, quantum ghost imaging is often performed with light sources that produce at most 10^6 photon pairs per second. The photons are typically detected using single-photon detectors such as avalanche photodiodes, and the correlation is performed numerically using digital methods. The spatial resolution of the ghost

image is determined by the transverse distance scale of the correlations between the two down-converted photons, which is determined by the phase-matching properties of the nonlinear crystal that produces the down-conversion. There is no intrinsic background to the ghost image, and the only intrinsic source of noise is that imposed by photon statistics.

In contrast, thermal ghost imaging uses two copies of a light field with limited transverse spatial coherence. The light source is typically a pseudothermal source produced by scattering laser light off a rotating ground glass plate [8–11], although true thermal sources have also been used [4,12]. In either case, the light source is usually much more intense than those used in quantum ghost imaging, which allows for a more rapid acquisition of the ghost image. The correlation that produces the ghost image can be performed using either analog or digital methods. The spatial resolution of the ghost image is determined by the transverse coherence (speckle size) of the light source. Ghost images are always formed on a large background, and the fluctuations in the background impose an intrinsic noise to the process of thermal ghost imaging.

II. THERMAL GHOST IMAGING

We first consider the analysis of the experimental configuration shown in Fig. 1. Spatially incoherent light is formed by scattering laser light off a rotating ground glass plate and is split into two beams by a beam splitter of intensity transmittance T and reflectance R . The light reflected by the beam splitter is incident on an object described by the intensity transmission function $T_{\text{obj}}(\mathbf{x}_B)$ and is then collected on a nonspatially resolving energy meter known as a bucket detector. The light transmitted by the beam splitter is incident on a spatially resolving detector such as a CCD.

Measurements of this sort are repeated K times, each time with a different speckle pattern. The ghost image of the object is then formed in the following manner. The pattern recorded by the CCD array is multiplied by the energy measured by the energy meter, and this result is summed over all of the K measurements. From Glauber's detection theory, we can write

*Present address: Rochester Optical Manufacturing Company, 1260 Lyell Ave., Rochester, NY 14606.

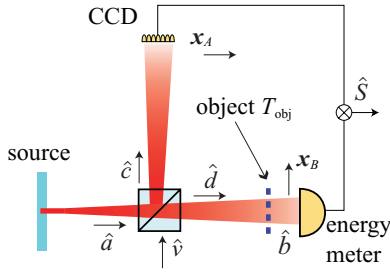


FIG. 1. (Color online) Typical thermal ghost imaging experimental setup.

the quantum operator for the ghost image signal for a pixel centered at point \mathbf{x} as

$$\hat{S}(\mathbf{x}) = \sum_{k=1}^K \int_{\Delta(\mathbf{x})} d\mathbf{x}_A \int d\mathbf{x}_B \hat{b}_{k,B}^\dagger \hat{c}_{k,A}^\dagger \hat{b}_{k,B} \hat{c}_{k,A}, \quad (1)$$

where $\Delta(\mathbf{x})$ is the area of the pixel, and $\hat{b}_{k,B}$ and $\hat{c}_{k,A}$ are the annihilation operators for the fields at point \mathbf{x}_B in the energy meter arm and at point \mathbf{x}_A in the CCD arm for the k th realization of the source. Here and throughout this paper we use the convention that the limits of integration of all integrals is the entire transverse plane unless otherwise noted. Thus, the integral over \mathbf{x}_B is taken to be the entire transverse plane, whereas the integral over \mathbf{x}_A is taken over the area of a pixel.

To proceed, we write the operators \hat{b} and \hat{c} , which act on the field in the detection planes, in terms of the operator \hat{a} , which acts on the field in the source plane. We accomplish this in two stages. First, the operators \hat{c} and \hat{d} that act on the field after the beam splitter are written in terms of the \hat{a}_k through the standard beam splitter relations given by

$$\hat{c}_{k,A} = i\sqrt{R}\hat{a}_{k,A} + \sqrt{T}\hat{v}_{k,A}, \quad (2)$$

$$\hat{d}_{k,B} = i\sqrt{R}\hat{v}_{k,B} + \sqrt{T}\hat{a}_{k,B}, \quad (3)$$

where \hat{v} is the annihilation operator for the mode entering the unused port of the beam splitter. The subscripts indicate that the operators are associated with the k th realization of the source at transverse field points \mathbf{x}_A and \mathbf{x}_B .

Second, we relate the operator \hat{b} that acts on the field entering the energy meter to the operator \hat{d} that acts on the field illuminating the object with intensity transmission function $T_{\text{obj}}(\mathbf{x}_B)$. As is typical in quantum descriptions of lossy processes [21], the operators are related through another beam splitter relation given by

$$\hat{b}_{k,B} = \sqrt{T_{\text{obj}}(\mathbf{x}_B)}\hat{d}_{k,B} + i\sqrt{1 - T_{\text{obj}}(\mathbf{x}_B)}\hat{v}'_{k,B}, \quad (4)$$

where \hat{v}' is an annihilation operator describing an auxiliary vacuum field. The subscripts have the same meaning as previously described. Both vacuum modes acted on by \hat{v} and \hat{v}' contribute to the noise of the ghost image at low photon levels.

A. Expected thermal ghost image

We next calculate the expectation value of the image signal operator \hat{S} . We assume that for each measurement the incoherent light field can be modeled as an independent Gaussian-Schell model (GSM) source. A GSM source can be

fully characterized by its second-order correlation function which we represent as

$$\langle \hat{a}_{k,A}^\dagger \hat{a}_{k,B} \rangle = \mathcal{N} \exp\left[-\frac{|\mathbf{x}_A|^2 + |\mathbf{x}_B|^2}{2w^2}\right] \exp\left[-\frac{|\mathbf{x}_A - \mathbf{x}_B|^2}{2\sigma^2}\right], \quad (5)$$

where \mathcal{N} is the mean number of photons per unit area at the center of the GSM beam, $\hat{a}_{k,(A,B)}$ is the annihilation operator as defined before, w gives the transverse size of the field, and σ describes the transverse spatial coherence of the field. For simplicity, w and σ are taken to be the sizes at the detection plane. Chan *et al.* [20] discuss how w and σ are modified by propagation in a ghost imaging experiment. All higher-order moments can be calculated in terms of the second-order moments through use of the Gaussian moment theorem [22].

The expected signal is given by the ensemble average of Eq. (1) over the K measurements. By applying Eqs. (1)–(5) as well as the Gaussian moment factoring theorem, we obtain

$$\langle \hat{S}(\mathbf{x}) \rangle = \mathcal{N}^2 R T K \int_{\Delta(\mathbf{x})} d\mathbf{x}_A \int d\mathbf{x}_B \exp\left[-\frac{|\mathbf{x}_A|^2 + |\mathbf{x}_B|^2}{w^2}\right] \times \left(1 + \exp\left[-\frac{|\mathbf{x}_A - \mathbf{x}_B|^2}{\sigma^2}\right]\right) T_{\text{obj}}(\mathbf{x}_B). \quad (6)$$

At this point, we make some assumptions that greatly simplify the ensuing development. First, we assume that the transverse extent of the illuminating speckle field is sufficiently large that its mean intensity is essentially constant over the transverse size of both the CCD array and the object (i.e., $\exp(-|\mathbf{x}_{A,B}|^2/w^2) \approx 1$). Second, we assume that the source has a sufficiently small transverse coherence length that the transmission of the object does not vary significantly on the scale of the coherence length (i.e., $T_{\text{obj}}(\mathbf{x})e^{-|\mathbf{x}-\mathbf{x}_0|^2/\sigma^2} \approx T_{\text{obj}}(\mathbf{x}_0)e^{-|\mathbf{x}-\mathbf{x}_0|^2/\sigma^2}$). Finally, we assume that each pixel of the CCD is sufficiently small that both $T_{\text{obj}}(\mathbf{x})$ and $e^{-|\mathbf{x}|^2/\sigma^2}$ are approximately constant over $\Delta(\mathbf{x})$. Using these assumptions, we can rewrite $\langle \hat{S}(\mathbf{x}) \rangle$ as

$$\langle \hat{S}(\mathbf{x}) \rangle = \mathcal{N}^2 R T K \Delta \left[\int d\mathbf{x} T_{\text{obj}}(\mathbf{x}) + \pi \sigma^2 T_{\text{obj}}(\mathbf{x}) \right], \quad (7)$$

where Δ is the area of one pixel of the CCD. This expression can be rewritten in a more intuitive fashion as

$$\langle \hat{S}(\mathbf{x}) \rangle = K N_\Delta [N_B + N_S T_{\text{obj}}(\mathbf{x})], \quad (8)$$

where $N_\Delta \equiv R \Delta \mathcal{N}$ is the average number of photons incident on one pixel of the CCD per realization, $N_B \equiv T \mathcal{N} \int d\mathbf{x} T_{\text{obj}}(\mathbf{x})$ is the average number of photons transmitted through the object and incident on the bucket detector per realization, and $N_S \equiv T \pi \sigma^2 \mathcal{N}$ is the average number of photons in one coherence area (i.e., in one “speckle”) incident on the object per realization.

Clearly, the image-carrying portion of the signal rides on an object-dependent background proportional to N_B . The mean background level can be determined by considering the total signal at a point \mathbf{x}_{bkgd} where $T_{\text{obj}}(\mathbf{x}_{\text{bkgd}}) = 0$. Thus, the background is given by

$$\langle \hat{S} \rangle_{\text{bkgd}} = K N_\Delta N_B. \quad (9)$$

Moreover, the image-carrying portion of the signal is given by

$$\langle \hat{S}(\mathbf{x}) \rangle_{\text{image}} = K N_{\Delta} N_S T_{\text{obj}}(\mathbf{x}). \quad (10)$$

From these results we see that the maximum signal-to-background ratio $\langle \hat{S} \rangle_{\text{image}} / \langle \hat{S} \rangle_{\text{bkgd}}$ is equal to N_S / N_B , which is inversely proportional to the number of speckles transmitted through the object. In other words, the contrast becomes degraded as the number of speckles transmitted through the object increases.

Intuitively we can understand this behavior as follows. The speckles incident on each pixel of the CCD are correlated only with the speckles passing through the corresponding position of the object. These speckles are responsible for the image-carrying portion of the signal. However, the bucket detector also detects uncorrelated speckles that pass through other regions of the object. These speckles lead to a background contribution to the signal. As the number of speckles transmitted through the object increases, the background increases linearly with no corresponding increase in the image-carrying portion of the signal. Hence, the contrast is reduced.

B. Signal-to-noise ratio

We next calculate the signal-to-noise ratio. In performing this calculation, we consider the ‘‘signal’’ to be the expectation value of the image-carrying portion of the signal, which we introduced as Eq. (10) in the previous section. The ‘‘noise’’ is defined in a root-mean-squared sense. As already mentioned, the image-carrying portion of the signal rides on a noisy background that is partially correlated with the image-carrying portion of the signal itself. Because of this correlation, noise in the image-carrying portion of the signal and noise in the background can partially cancel each other when the background is subtracted.

To account for this behavior, we introduce the operator \hat{S}_{image} for the background-subtracted image. We first note that the background at image point \mathbf{x} is given by the product of the average signal of the energy meter with the average signal of the CCD pixel centered at \mathbf{x} . We can thus write the operator for the background portion of the signal as

$$\hat{S}_{\text{bkgd}}(\mathbf{x}) = \frac{1}{K} \sum_{m,n=1}^K \int_{\Delta(\mathbf{x})} d\mathbf{x}_A \int d\mathbf{x}_B \hat{b}_{m,B}^{\dagger} \hat{c}_{n,A}^{\dagger} \hat{b}_{m,B} \hat{c}_{n,A}. \quad (11)$$

Thus, the image-carrying portion of the signal is described by the background-subtracted image operator,

$$\hat{S}_{\text{image}}(\mathbf{x}) = \frac{K}{K-1} [\hat{S}(\mathbf{x}) - \hat{S}_{\text{bkgd}}(\mathbf{x})], \quad (12)$$

where $K/(K-1)$ is the usual factor needed to obtain an unbiased estimate of the imaging signal. Of course, in the usual limit of large K this factor approaches unity. Taking the ensemble average of Eq. (12) and substituting in Eqs. (1)–(5) and (9), the result shown in Eq. (10) is recovered as expected. The variance of \hat{S}_{image} is given by

$$(\Delta \hat{S})_{\text{image}}^2 = \frac{K^2}{(K-1)^2} [(\Delta \hat{S})^2 + (\Delta \hat{S})_{\text{bkgd}}^2 - 2\text{cov}(\hat{S}, \hat{S}_{\text{bkgd}})], \quad (13)$$

where $(\Delta \hat{S})^2$ and $(\Delta \hat{S})_{\text{bkgd}}^2$ are the variances of \hat{S} and \hat{S}_{bkgd} . The covariance between the total signal and the background is given by $\text{cov}(\hat{S}, \hat{S}_{\text{bkgd}})$. The calculation of the $(\Delta \hat{S})_{\text{image}}^2$ is straightforward but lengthy and is presented in the appendix. Through use of Eq. (A15) of the appendix, and in the common situation in which $K \gg 1$, we find that the signal-to-noise ratio is given by

$$R_{\text{th}}^{\text{SN}} = \frac{\langle \hat{S}(\mathbf{x}) \rangle_{\text{image}}}{(\Delta \hat{S})_{\text{image}}} = \sqrt{K N_{\Delta}} \frac{N_S T_{\text{obj}}(\mathbf{x})}{[\alpha_1 + \alpha_2 + \alpha_3]^{1/2}}, \quad (14)$$

where α_m are quantities that depend on the m th power of the the photon number \mathcal{N} and are given by

$$\begin{aligned} \alpha_1 &\equiv N_B + N_S T_{\text{obj}}(\mathbf{x}), \\ \alpha_2 &\equiv N_{\Delta} N_B + N_S N_B^{(2)} + 2N_S T_{\text{obj}}(\mathbf{x}) \left[\frac{4}{3} N_S T_{\text{obj}}(\mathbf{x}) + N_{\Delta} \right], \\ \alpha_3 &\equiv N_{\Delta} N_S \left[N_B^{(2)} + \frac{25}{3} N_S T_{\text{obj}}^2(\mathbf{x}) \right], \end{aligned}$$

where $N_B^{(2)} \equiv T \mathcal{N} \int d\mathbf{x} T_{\text{obj}}^2(\mathbf{x})$. Clearly, for a binary object $N_B^{(2)} = N_B$.

Although this result is in general quite complicated, its limiting cases lead to simple expressions. For example, we first assume that the object is highly transmitting such that $N_B, N_B^{(2)} \gg N_S$, and we furthermore assume that $N_S \gg N_{\Delta}$. Moreover, we consider an object point where $T_{\text{obj}}(\mathbf{x}) = 1$. Then, in the low-photon-flux limit (much fewer than one photon per speckle) for which α_1 dominates, $R_{\text{th}}^{\text{SN}} \rightarrow N_S [K N_{\Delta} / N_B]^{1/2}$. This result can be understood intuitively by recognizing that, in the low-photon-flux limit, the signals from both the energy meter and the CCD are dominated by shot noise. Thus, the noise of the product of the detected signals is given approximately by $(N_{\Delta} N_B)^{1/2}$, which leads directly to the quoted result. In the high-photon-flux limit, where α_3 dominates, $R_{\text{th}}^{\text{SN}} \rightarrow [K N_S / N_B^{(2)}]^{1/2}$, which is independent of the average photon flux. In both cases, when the object is binary (i.e., $N_B = N_B^{(2)}$), the signal-to-noise ratio varies inversely with the square root of the transmitting area of the object, which agrees with the results found in Ref. [13].

III. QUANTUM GHOST IMAGING

In quantum ghost imaging, the object and spatially resolving detector array are illuminated by photons produced by the process of spontaneous parametric down-conversion (SPDC), and coincidence detections events between the pixels on the detector array and bucket detector are recorded. In our analysis, we consider the biphoton limit of type-II SPDC and neglect the contributions of the emission of multiple pairs. We assume that K biphotons are used to create the image. Since the K -photon pairs are independent of one another, the wave function of the ensemble of biphotons can be written as the tensor product of K -biphoton states (i.e., $|\psi\rangle^{\otimes K}$) where

$$\begin{aligned} |\psi\rangle &= \frac{1}{\pi \sigma w} \int d\mathbf{x}_A \int d\mathbf{x}_B \exp \left[-\frac{|\mathbf{x}_A + \mathbf{x}_B|^2}{2w^2} \right] \\ &\times \exp \left[-\frac{|\mathbf{x}_A - \mathbf{x}_B|^2}{2\sigma^2} \right] \hat{b}_A^{\dagger} \hat{c}_B^{\dagger} |0,0\rangle \end{aligned} \quad (15)$$

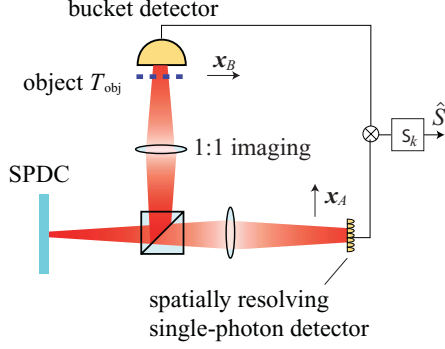


FIG. 2. (Color online) Typical experimental setup for performing quantum ghost imaging. SPDC, spontaneous parametric down-converter.

is the biphoton wave function of one realization, where w is the transverse size of the pump field, and σ determines transverse spatial coherence of the biphoton [23]. The operators \hat{b}'_A and \hat{c}_B are the annihilation operators for signal and idler fields at the point with transverse coordinates \mathbf{x}_A and \mathbf{x}_B for a given realization.

A typical quantum ghost imaging setup is shown in Fig. 2. Since in type-II SPDC the emitted photons can be deterministically separated at a polarizing beam splitter, we do not need to consider contributions due to the vacuum mode at the unused port of the beam splitter. For simplicity, we assume that exit face of the nonlinear crystal is imaged onto both the object plane and the plane of the detector array with unit magnification. Thus, the wave function given in Eq. (15) describes the two-photon state of the signal photon at the object plane and the idler photon on the plane of the detector array. We note that quantum ghost imaging can be performed using other lens configurations. Ref. [20] discusses how to rescale $\mathbf{x}_{A,B}$, σ , and w in Eq. (15) to account for these configurations.

A. Expected quantum ghost image

Proceeding in the same manner as in Sec. II A, we calculate the expected signal level for a quantum ghost image produced by K biphotons. Using Eqs. (1) and (15), we find that

$$\langle \hat{S}(\mathbf{x}) \rangle = \frac{K}{\pi \sigma^2 w^2} \int_{\Delta(\mathbf{x})} d\mathbf{x}_A \int d\mathbf{x}_B \exp \left[-\frac{|\mathbf{x}_A + \mathbf{x}_B|^2}{w^2} \right] \times \exp \left[-\frac{|\mathbf{x}_A - \mathbf{x}_B|^2}{\sigma^2} \right] T_{\text{obj}}(\mathbf{x}_B). \quad (16)$$

By adjusting the pump beam size and the crystal length, we can control w and σ . Making the same set of assumptions for the relative sizes of w , σ , Δ , and the extent of T_{obj} as detailed in Sec. II A, we can write the expected quantum ghost image as

$$\langle \hat{S}(\mathbf{x}) \rangle = K p_{\Delta} T_{\text{obj}}(\mathbf{x}), \quad (17)$$

where $p_{\Delta} \equiv \Delta/(\pi w^2)$ is the probability that a photon falls onto a specific pixel of area Δ of the detector array. From this expression we see that, unlike as in thermal ghost imaging, a quantum ghost image does not rest on a background. This

behavior follows from the strong spatial correlations that each photon pair exhibits. A coincidence is registered only when the signal photon is transmitted through the object and the idler photon is incident on the corresponding pixel of the detector array.

B. Signal-to-noise ratio

We define the signal-to-noise ratio in a manner similar to that of Sec. II B. The signal is given by Eq. (17). Since the quantum ghost image does not rest on a background, no background-subtraction methods need to be implemented. Thus, the noise is calculated as the root-mean-squared deviation of the imaging operator \hat{S} from the expected image signal. We calculate the variance of S from $\langle (S - \langle S \rangle)^2 \rangle$ using the state given in Eq. (15) and find that under the usual approximations,

$$(\Delta \hat{S})^2 = K p_{\Delta} T_{\text{obj}}(\mathbf{x}) [1 - p_{\Delta} T_{\text{obj}}(\mathbf{x})] \approx K p_{\Delta} T_{\text{obj}}(\mathbf{x}), \quad (18)$$

where the final approximation is justified since $p_{\Delta} \ll 1$ in the biphoton limit of parametric down-conversion. This result is not surprising since the quantum image is formed by counting coincident detection events, whose noise is characterized by Poissonian noise, for which the variance is equal to the mean. Thus, the signal-to-noise ratio is found to be

$$R_{\text{qu}}^{\text{SN}} = \frac{\langle \hat{S} \rangle}{(\Delta \hat{S})} = \sqrt{K p_{\Delta} T_{\text{obj}}(\mathbf{x})}. \quad (19)$$

As with thermal ghost imaging, the SNR of a quantum ghost image can be made arbitrarily large by increasing K . Unlike the SNR of a thermal ghost image, the SNR of a quantum ghost image depends only on the transmittance of the object at the point of interest. Recall that, in contrast, the noise of a thermal ghost image degrades as the total transmittance of the entire object increases.

IV. DISCUSSION AND CONCLUSIONS

In this section we compare the performance of thermal and quantum ghost imaging under various different circumstances.

We first compare the performance of the two methods under the assumption that the illumination levels used in the two methods are the same. In particular, we assume that the average number of photons incident on one pixel of the detector array per realization for the thermal case N_{Δ} is equal to the average number of photons p_{Δ} for the quantum case. By assumption, $p_{\Delta} \ll 1$, because in the quantum case there is only one photon per measurement and there are many pixels. We thus make use of the results for the low-photon-flux approximation of Eq. (14) for the thermal case and we make use of Eq. (19) for the quantum case. The ratio of the SNRs in the two cases is thus given by

$$\frac{R_{\text{th}}^{\text{SN}}}{R_{\text{qu}}^{\text{SN}}} = \frac{N_S \sqrt{T_{\text{obj}}(\mathbf{x})}}{[N_B + N_S T_{\text{obj}}(\mathbf{x})]^{1/2}}. \quad (20)$$

This ratio is less than or equal to $\sqrt{N_S}$. Since we assumed that only one photon interrogates the object, N_S must be very much smaller than unity and we conclude that $R_{\text{th}}^{\text{SN}} \ll R_{\text{qu}}^{\text{SN}}$. Thus, quantum ghost imaging always yields a superior image

when the object is illuminated at the single-photon level for each individual measurement.

However, as we noted in the introduction, one of the advantages of thermal ghost imaging over quantum ghost imaging is its ability to operate at higher intensities and thus produce larger signal-to-noise ratios. Indeed, we showed in Sec. II B that when imaging a binary object at high intensities, $R_{\text{th}, \mathcal{N} \gg 1}^{\text{SN}} = [KN_S/N_B]^{1/2}$. If we interpret the quantity N_B/N_S as the number of speckles transmitted through the object and $1/p_\Delta$ as the total number of illuminated pixels in the object plane, it follows that $N_S/N_B < p_\Delta$. Using these results together with Eq. (19), we find that $R_{\text{th}, \mathcal{N} \gg 1}^{\text{SN}} > R_{\text{qu}}^{\text{SN}}$ and conclude that thermal ghost imaging at high intensities always outperforms quantum ghost imaging.

It is useful then to determine the critical illumination level for which thermal ghost imaging yields the same SNR as quantum ghost imaging. For reasons that we justify below, we use the low-photon-flux approximation to $R_{\text{th}}^{\text{SN}}$, that is, we assume that $N_S \ll 1$. We also make the simplifying assumption of a highly transmitting object so that $N_B \gg N_S$. We consider the signal at a fully transmitting point on the object such that $T_{\text{obj}}(\mathbf{x}) = 1$. We then solve for the value of N_S for which $R_{\text{th}}^{\text{SN}} = R_{\text{qu}}^{\text{SN}}$. We thereby find that the two imaging methods perform comparably whenever the average number of photons per speckle in the field illuminating the object satisfies the condition,

$$N_{S, \text{crit}} = \sqrt{A/(\pi w^2)}, \quad (21)$$

where $A \equiv N_B/\mathcal{N}$ is equal to the transmitting area of the object for a binary object. We note that this ratio is often much smaller than unity, so we were justified in using the low-photon flux approximation to $R_{\text{th}}^{\text{SN}}$. We conclude that even for very modest illumination intensities for which $N_S > N_{S, \text{crit}}$, thermal ghost imaging produces better images than quantum ghost imaging.

Another way to compare the two imaging methods is to compare the resulting SNRs when the same, fixed number of photons is used to illuminate the object. This sort of comparison might be relevant under circumstances for which photons are very costly or in which one wants to minimize the illumination levels for reasons of stealth. Recall that thermal ghost imaging uses $\pi w^2 \mathcal{N} K$ photons to obtain the image, whereas quantum ghost imaging uses $2K$ photons total. Figure 3 shows a plot of the SNR as a function of the total number of photons used for the two different methods. For a thermal ghost image we can increase the total number of photons used in two ways. One way is to increase the intensity of the light illuminating the object (i.e., by increasing \mathcal{N}). Alternatively, we can increase the total number of photons by increasing the number of realizations K . In quantum ghost imaging, we can increase the number of photons used to obtain the image only by increasing K , because by assumption the biphoton source produces only one photon pair at a time. The three thermal ghost imaging curves in the figure assume different fixed values of K ; in each case the illumination level \mathcal{N} is allowed to vary to control the total number of photons used to obtain the image. From the plot it is clear that quantum ghost imaging always performs better when only a fixed number of photons are available to illuminate

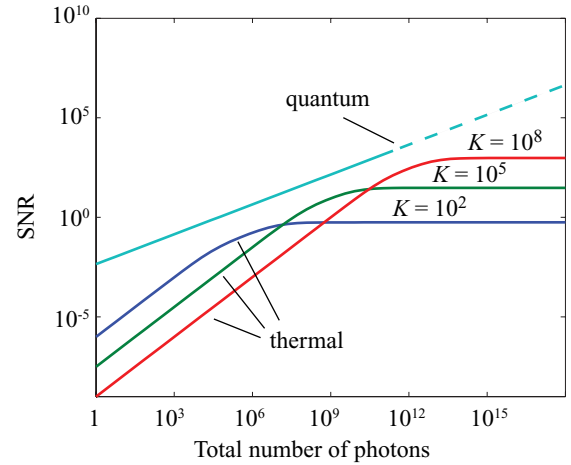


FIG. 3. (Color online) Signal-to-noise (SNR) ratio achievable by either quantum or thermal ghost imaging plotted against the total number of photons used in the illuminating field. The dotted portion of the quantum imaging curve cannot be realistically attained using current biphoton sources but is shown for completeness. The three curves for thermal ghost imaging correspond to different numbers K of realizations (speckle patterns) that are averaged together to form the ghost image. We take the object to be a binary object with total transmitting area of 10^4 pixels and the characteristic area of a speckle to be $\pi\sigma^2 = 100$ pixels. We assume that the illumination beam has a cross-sectional area of 10^5 pixels.

the object. We note that using current biphoton sources, quantum ghost images with SNRs requiring $K \gtrsim 10^{12}$ are not practical, in which cases thermal ghost imaging must be used.

The results presented in this article are formally consistent with those of Erkmén and Shapiro [13], although we have chosen a different form of graphical display to illustrate our results and have chosen different special cases to treat, and thus different insight is provided by our analysis. Recent calculations demonstrate that, for identical values of the spatial coherence parameter σ at the source plane in comparable quantum and thermal ghost imaging systems, both systems produce images with the same resolution [20]. The present analysis concludes, however, that a typical quantum ghost imaging system yields a poorer-quality image in terms of its SNR than a thermal ghost image system. A thermal ghost imaging system needs only a slightly higher average illumination intensity to outperform a quantum ghost imaging system. However, in photon-limited situations, quantum ghost imaging systems perform substantially better than thermal ghost imaging systems.

ACKNOWLEDGMENTS

The authors gratefully acknowledge support by means of an Army Research Office–Multidisciplinary University Research Initiative award.

APPENDIX

We now work out the variance of the thermal ghost imaging signal in detail, using the assumptions made in the body of the

text. The variance of the total signal $(\Delta\hat{S})^2$, introduced in Eq. (13), is given by

$$(\Delta\hat{S})^2 = \sum_{j,k=1}^K \iint_{\Delta(\mathbf{x})} d\mathbf{x}_A d\mathbf{x}'_A \iint d\mathbf{x}_B d\mathbf{x}'_B \times [(\hat{b}_{j,B}^\dagger \hat{b}_{j,B} \hat{c}_{j,A}^\dagger \hat{c}_{j,A} \hat{b}_{k,B}^\dagger \hat{b}_{k,B} \hat{c}_{k,A'}^\dagger \hat{c}_{k,A'}) - (\hat{b}_B^\dagger \hat{b}_B \hat{c}_A^\dagger \hat{c}_A) (\hat{b}_{B'}^\dagger \hat{b}_{B'} \hat{c}_{A'}^\dagger \hat{c}_{A'})]. \quad (\text{A1})$$

When $j \neq k$, the term in brackets will vanish. The remaining K terms will involve expectation values independent of the summation index, so the resulting expression can be written as

$$(\Delta\hat{S})^2 = K \iint_{\Delta(\mathbf{x})} d\mathbf{x}_A d\mathbf{x}'_A \iint d\mathbf{x}_B d\mathbf{x}'_B \times [(\hat{n}_B \hat{n}_A \hat{n}_{B'} \hat{n}_{A'}) - \langle \hat{n}_B \hat{n}_A \rangle \langle \hat{n}_{B'} \hat{n}_{A'} \rangle], \quad (\text{A2})$$

where $\hat{n}_i = \hat{b}_i^\dagger \hat{b}_i$ for $i = B, B'$ and $\hat{n}_j = \hat{c}_j^\dagger \hat{c}_j$ for $j = A, A'$.

We treat the variance of the background portion of the signal in a similar fashion:

$$(\Delta\hat{S})_{\text{bgkd}}^2 = \frac{1}{K^2} \sum_{j,k,r,s=1}^K \iint_{\Delta(\mathbf{x})} d\mathbf{x}_A d\mathbf{x}'_A \iint d\mathbf{x}_B d\mathbf{x}'_B \times [(\hat{b}_{j,B}^\dagger \hat{b}_{j,B} \hat{c}_{k,A}^\dagger \hat{c}_{k,A} \hat{b}_{r,B'}^\dagger \hat{b}_{r,B'} \hat{c}_{s,A'}^\dagger \hat{c}_{s,A'}) - (\hat{b}_{j,B}^\dagger \hat{b}_{j,B} \hat{c}_{k,A}^\dagger \hat{c}_{k,A}) (\hat{b}_{r,B'}^\dagger \hat{b}_{r,B'} \hat{c}_{s,A'}^\dagger \hat{c}_{s,A'})]. \quad (\text{A3})$$

When $j, k \neq r, s$, the term in brackets vanish. The remaining terms can be grouped into instances when $(j = k = r = s), (j \neq k = r = s), (j = k \neq r = s)$, etc., yielding

$$\begin{aligned} (\Delta\hat{S})_{\text{bgkd}}^2 &= \frac{1}{K^2} \iint_{\Delta(\mathbf{x})} d\mathbf{x}_A d\mathbf{x}'_A \iint d\mathbf{x}_B d\mathbf{x}'_B \\ &\times \{K[(\hat{n}_B \hat{n}_A \hat{n}_{B'} \hat{n}_{A'}) - \langle \hat{n}_B \hat{n}_A \rangle \langle \hat{n}_{B'} \hat{n}_{A'} \rangle] \\ &+ 2K(K-1)[\langle \hat{n}_B \rangle \langle \hat{n}_{B'} \hat{n}_A \hat{n}_{A'} \rangle + \langle \hat{n}_A \rangle \langle \hat{n}_B \hat{n}_{B'} \hat{n}_{A'} \rangle \\ &- 2\langle \hat{n}_A \rangle \langle \hat{n}_B \rangle \langle \hat{n}_{B'} \hat{n}_{A'} \rangle] + K(K-1)[\langle \hat{n}_B \hat{n}_{B'} \rangle \langle \hat{n}_A \hat{n}_{A'} \rangle \\ &+ \langle \hat{n}_B \hat{n}_A \rangle \langle \hat{n}_{A'} \hat{n}_{B'} \rangle - 2\langle \hat{n}_B \rangle \langle \hat{n}_{B'} \rangle \langle \hat{n}_A \rangle \langle \hat{n}_{A'} \rangle] \\ &+ K(K-1)(K-2)\langle \hat{n}_A \rangle \langle \hat{n}_{A'} \rangle [\langle \hat{n}_B \hat{n}_{B'} \rangle - \langle \hat{n}_B \rangle \langle \hat{n}_{B'} \rangle] \\ &+ 2K(K-1)(K-2)\langle \hat{n}_B \rangle \langle \hat{n}_A \rangle [\langle \hat{n}_{B'} \hat{n}_{A'} \rangle - \langle \hat{n}_{B'} \rangle \langle \hat{n}_{A'} \rangle] \\ &+ K(K-1)(K-2)\langle \hat{n}_B \rangle \langle \hat{n}_{B'} \rangle [\langle \hat{n}_A \hat{n}_{A'} \rangle - \langle \hat{n}_A \rangle \langle \hat{n}_{A'} \rangle] \}. \end{aligned} \quad (\text{A4})$$

Finally, the covariance between the total signal and the background portion can be written,

$$\text{cov}(\hat{S}, \hat{S}_{\text{bgkd}}) = \frac{1}{K} \sum_{j,r,s=1}^K \iint_{\Delta(\mathbf{x})} d\mathbf{x}_A d\mathbf{x}'_A \iint d\mathbf{x}_B d\mathbf{x}'_B \times [(\hat{b}_{j,B}^\dagger \hat{b}_{j,B} \hat{c}_{j,A}^\dagger \hat{c}_{j,A} \hat{b}_{r,B'}^\dagger \hat{b}_{r,B'} \hat{c}_{s,A'}^\dagger \hat{c}_{s,A'}) - (\hat{b}_B^\dagger \hat{b}_B \hat{c}_A^\dagger \hat{c}_A) (\hat{b}_{B'}^\dagger \hat{b}_{B'} \hat{c}_{s,A'}^\dagger \hat{c}_{s,A'})]. \quad (\text{A5})$$

As in the preceding equations, we can simplify this expression to read

$$\text{cov}(\hat{S}, \hat{S}_{\text{bgkd}}) = \frac{1}{K} \iint_{\Delta(\mathbf{x})} d\mathbf{x}_A d\mathbf{x}'_A \iint d\mathbf{x}_B d\mathbf{x}'_B \times \{K[(\hat{n}_B \hat{n}_A \hat{n}_{B'} \hat{n}_{A'}) - \langle \hat{n}_B \hat{n}_A \rangle \langle \hat{n}_{B'} \hat{n}_{A'} \rangle]\}$$

$$\begin{aligned} &+ K(K-1)[\langle \hat{n}_B \rangle \langle \hat{n}_{B'} \hat{n}_A \hat{n}_{A'} \rangle \\ &+ \langle \hat{n}_A \rangle \langle \hat{n}_B \hat{n}_{B'} \hat{n}_{A'} \rangle - 2\langle \hat{n}_A \rangle \langle \hat{n}_B \rangle \langle \hat{n}_{B'} \hat{n}_{A'} \rangle]. \end{aligned} \quad (\text{A6})$$

Substituting Eqs. (A2), (A4), and (A6) into Eq. (13), we find

$$\begin{aligned} (\Delta\hat{S})_{\text{image}}^2 &= K \iint_{\Delta(\mathbf{x})} d\mathbf{x}_A d\mathbf{x}'_A \iint d\mathbf{x}_B d\mathbf{x}'_B \\ &\times \left\{ [(\hat{n}_B \hat{n}_A \hat{n}_{B'} \hat{n}_{A'}) - \langle \hat{n}_B \hat{n}_A \rangle \langle \hat{n}_{B'} \hat{n}_{A'} \rangle] \right. \\ &- 2[\langle \hat{n}_B \rangle \langle \hat{n}_{B'} \hat{n}_A \hat{n}_{A'} \rangle + \langle \hat{n}_A \rangle \langle \hat{n}_B \hat{n}_{B'} \hat{n}_{A'} \rangle \\ &- 2\langle \hat{n}_A \rangle \langle \hat{n}_B \rangle \langle \hat{n}_{B'} \hat{n}_{A'} \rangle] + \frac{K-2}{K-1} [\langle \hat{n}_A \rangle \langle \hat{n}_{A'} \rangle \\ &\times (\langle \hat{n}_B \hat{n}_{B'} \rangle - \langle \hat{n}_B \rangle \langle \hat{n}_{B'} \rangle) + 2\langle \hat{n}_B \rangle \langle \hat{n}_{A'} \rangle \\ &\times (\langle \hat{n}_B \hat{n}_{A'} \rangle - \langle \hat{n}_{B'} \rangle \langle \hat{n}_A \rangle) + \langle \hat{n}_B \rangle \langle \hat{n}_{B'} \rangle (\langle \hat{n}_A \hat{n}_{A'} \rangle \\ &- \langle \hat{n}_A \rangle \langle \hat{n}_{A'} \rangle)] + \frac{1}{K-1} [\langle \hat{n}_B \hat{n}_{B'} \rangle \langle \hat{n}_A \hat{n}_{A'} \rangle \\ &\left. + \langle \hat{n}_B \hat{n}_{A'} \rangle \langle \hat{n}_A \hat{n}_{B'} \rangle - 2\langle \hat{n}_B \rangle \langle \hat{n}_{B'} \rangle \langle \hat{n}_A \rangle \langle \hat{n}_{A'} \rangle] \right\}. \end{aligned} \quad (\text{A7})$$

To proceed, we apply normal ordering and our beam-splitter relations. We substitute the following set of relations for the correlation functions into the above equation:

$$\begin{aligned} &\langle \hat{n}_B \hat{n}_A \hat{n}_{B'} \hat{n}_{A'} \rangle \\ &\rightarrow RTT_{\text{obj}}(\mathbf{x}_B) \delta(\mathbf{x}_A - \mathbf{x}'_A) \delta(\mathbf{x}_B - \mathbf{x}'_B) \langle : \hat{n}_B \hat{n}_A : \rangle \\ &+ R^2 T T_{\text{obj}}(\mathbf{x}_B) \delta(\mathbf{x}_B - \mathbf{x}'_B) \langle : \hat{n}_B \hat{n}_A \hat{n}_{A'} : \rangle \\ &+ RT^2 T_{\text{obj}}(\mathbf{x}_B) T_{\text{obj}}(\mathbf{x}'_B) \delta(\mathbf{x}_A - \mathbf{x}'_A) \langle : \hat{n}_B \hat{n}_{B'} \hat{n}_{A'} : \rangle \\ &+ R^2 T^2 T_{\text{obj}}(\mathbf{x}_B) T_{\text{obj}}(\mathbf{x}'_B) \langle : \hat{n}_B \hat{n}_{B'} \hat{n}_A \hat{n}_{A'} : \rangle, \\ &\langle \hat{n}_B \hat{n}_A \hat{n}_{A'} \rangle \rightarrow RTT_{\text{obj}}(\mathbf{x}'_B) \delta(\mathbf{x}_A - \mathbf{x}'_A) \langle : \hat{n}_B \hat{n}_A : \rangle \\ &+ R^2 T T_{\text{obj}}(\mathbf{x}'_B) \langle : \hat{n}_B \hat{n}_A \hat{n}_{A'} : \rangle, \end{aligned} \quad (\text{A8})$$

$$\begin{aligned} &\langle \hat{n}_B \hat{n}_{B'} \hat{n}_{A'} \rangle \rightarrow RTT_{\text{obj}}(\mathbf{x}_B) \delta(\mathbf{x}_B - \mathbf{x}'_B) \langle : \hat{n}_B \hat{n}_{A'} : \rangle \\ &+ RT^2 T_{\text{obj}}(\mathbf{x}_B) T_{\text{obj}}(\mathbf{x}'_B) \langle : \hat{n}_B \hat{n}_{B'} \hat{n}_{A'} : \rangle, \\ &\langle \hat{n}_B \hat{n}_A \rangle \rightarrow RTT_{\text{obj}}(\mathbf{x}_B) \langle : \hat{n}_B \hat{n}_A : \rangle, \end{aligned} \quad (\text{A9})$$

$$\begin{aligned} &\langle \hat{n}_B \hat{n}_{B'} \rangle \rightarrow TT_{\text{obj}}(\mathbf{x}_B) \delta(\mathbf{x}_B - \mathbf{x}'_B) \langle \hat{n}_B \rangle \\ &+ T^2 T_{\text{obj}}(\mathbf{x}_B) T_{\text{obj}}(\mathbf{x}'_B) \langle : \hat{n}_B \hat{n}_{B'} : \rangle, \end{aligned} \quad (\text{A10})$$

$$\langle \hat{n}_A \hat{n}_{A'} \rangle \rightarrow R \delta(\mathbf{x}_A - \mathbf{x}'_A) \langle \hat{n}_A \rangle + R^2 \langle : \hat{n}_A \hat{n}_{A'} : \rangle, \quad (\text{A11})$$

$$\langle \hat{n}_B \rangle \rightarrow TT_{\text{obj}}(\mathbf{x}_B) \langle \hat{n}_B \rangle, \quad (\text{A12})$$

$$\langle \hat{n}_A \rangle \rightarrow R \langle \hat{n}_A \rangle, \quad (\text{A13})$$

where $\hat{n}_i = \hat{a}_i^\dagger \hat{a}_i$ for $i = A, B, A', B'$ on the right-hand side of the relations.

We expand the normally ordered correlation functions using the Gaussian moment factoring theorem and implement the approximations mentioned previously to obtain

$$\begin{aligned} (\Delta\hat{S})_{\text{image}}^2 &= KN_\Delta \left\{ N_B + N_S T_{\text{obj}}(\mathbf{x}) + N_S N_B^{(2)} + 2N_\Delta N_S T_{\text{obj}}(\mathbf{x}) \right. \\ &+ \frac{8}{3} N_S^2 T_{\text{obj}}^2(\mathbf{x}) + \frac{25}{3} N_\Delta N_S^2 T_{\text{obj}}^2(\mathbf{x}) - 2N_\Delta N_S N_B T_{\text{obj}}(\mathbf{x}) \\ &\left. - N_B^2 (N_\Delta + 1) \right\} + K \frac{K-1}{K-2} N_\Delta \{ N_B^2 (N_\Delta + 1) \} \end{aligned}$$

$$\begin{aligned}
& + N_{\Delta} N_B + N_{\Delta} N_S N_B^{(2)} + 2N_{\Delta} N_S N_B T_{\text{obj}}(\mathbf{x}) \} \\
& + \frac{K}{K-1} N_{\Delta} \{ N_B + N_B^2 + N_S N_B^{(2)} \\
& + N_{\Delta} [2N_B + 2N_S N_B^{(2)} + 2N_S N_B T_{\text{obj}}(\mathbf{x}) \\
& + N_B^2 + N_S^2 T_{\text{obj}}^2(\mathbf{x})] \}. \tag{A14}
\end{aligned}$$

In the usual limit of large K , this expression simplifies to

$$\begin{aligned}
(\Delta \hat{S})_{\text{image}}^2 = & K N_{\Delta} \{ (N_{\Delta} + 1)(N_B + N_S N_B^{(2)}) + N_S T_{\text{obj}}(\mathbf{x}) \\
& \times [1 + 2N_{\Delta} + \frac{1}{3} N_S T_{\text{obj}}(\mathbf{x})(8 + 25N_{\Delta})] \}. \tag{A15}
\end{aligned}$$

-
- [1] T. B. Pittman, Y. H. Shih, D. V. Strekalov, and A. V. Sergienko, *Phys. Rev. A* **52**, R3429 (1995).
- [2] T. B. Pittman, D. V. Strekalov, D. N. Klyshko, M. H. Rubin, A. V. Sergienko, and Y. H. Shih, *Phys. Rev. A* **53**, 2804 (1996).
- [3] A. Gatti, E. Brambilla, and L. A. Lugiato, *Phys. Rev. Lett.* **90**, 133603 (2003).
- [4] D. Zhang, Y. Zhai, L. Wu, and X. Chen, *Opt. Lett.* **30**, 2354 (2005).
- [5] A. F. Abouraddy, P. R. Stone, A. V. Sergienko, B. E. A. Saleh, and M. C. Teich, *Phys. Rev. Lett.* **93**, 213903 (2004).
- [6] B. Jack, J. Leach, J. Romero, S. Franke-Arnold, M. Ritsch-Marte, S. M. Barnett, and M. J. Padgett, *Phys. Rev. Lett.* **103**, 083602 (2009).
- [7] F. Ferri, D. Magatti, A. Gatti, M. Bache, E. Brambilla, and L. A. Lugiato, *Phys. Rev. Lett.* **94**, 183602 (2005).
- [8] G. Scarcelli, A. Valencia, and Y. Shih, *Phys. Rev. A* **70**, 051802(R) (2004).
- [9] F. Ferri, D. Magatti, A. Gatti, M. Bache, E. Brambilla, and L. A. Lugiato, *Phys. Rev. Lett.* **94**, 183602 (2005).
- [10] L. Basano and P. Ottonello, *Appl. Phys. Lett.* **89**, 091109 (2006).
- [11] R. Meyers, K. S. Deacon, and Y. Shih, *Phys. Rev. A* **77**, 041801 (2008).
- [12] X. Chen, Q. Liu, K. Luo, and L. Wu, *Opt. Lett.* **34**, 695 (2009).
- [13] B. I. Erkmen and J. H. Shapiro, *Phys. Rev. A* **79**, 023833 (2009).
- [14] B. I. Erkmen and J. H. Shapiro, *Phys. Rev. A* **78**, 023835 (2008).
- [15] A. Gatti, E. Brambilla, M. Bache, and L. A. Lugiato, *Phys. Rev. Lett.* **93**, 093602 (2004).
- [16] M. D'Angelo, A. Valencia, M. H. Rubin, and Y. Shih, *Phys. Rev. A* **72**, 013810 (2005).
- [17] L. Basano and P. Ottonello, *Opt. Express* **15**, 12386 (2007).
- [18] I. F. Santos, J. G. Aguirre-Gómez, and S. Pádua, *Phys. Rev. A* **77**, 043832 (2008).
- [19] L.-G. Wang, S. Qamar, S.-Y. Zhu, and M. S. Zubairy, *Phys. Rev. A* **79**, 033835 (2009).
- [20] K. W. C. Chan, M. N. O'Sullivan, and R. W. Boyd, *Phys. Rev. A* **79**, 033808 (2009).
- [21] H. P. Yuen and J. H. Shapiro, in *Coherence and Quantum Optics IV*, edited by L. Mandel and E. Wolf (Plenum, New York, 1978), p. 719.
- [22] L. Mandel and E. Wolf, *Optical Coherence and Quantum Optics* (Cambridge University Press, New York, 1995).
- [23] C. K. Law and J. H. Eberly, *Phys. Rev. Lett.* **92**, 127903 (2004).